Title
Patterned photocrosslinking to establish stiffness anisotropies in fibrous 3D hydrogels

Permalink
https://escholarship.org/uc/item/5gz1q7db

Authors
Jagiełło, Alicja
Hu, Qingda
Castillo, Ulysses
et al.

Publication Date
2022-03-01

DOI
10.1016/j.actbio.2021.12.028

Peer reviewed

Patterned photocrosslinking to establish stiffness anisotropies in fibrous 3D hydrogels

Alicja Jagiełło[1], **Qingda Hu**[1,2], **Ulysses Castillo**[1], **Elliot Botvinick**[1,2,3,4]

[1.] Department of Biomedical Engineering, University of California, Irvine, CA 92697-2715

[2.] Center for Complex Biological Systems, University of California, Irvine, CA 92697-2280

[3.] Beckman Laser Institute and Medical Clinic, University of California, Irvine, CA 92612

[4.] The Edwards Lifesciences Foundation Cardiovascular Innovation and Research Center, University of California, Irvine, CA 92697-2730

Abstract

Cells are known to constantly interact with their local extracellular matrix (ECM) and respond to a variety of biochemical and mechanical cues received from the ECM. Nonetheless, comprehensive understanding of cell-ECM interactions has been elusive. Many studies rely on analysis of cell behavior on 2D substrates, which do not reflect a natural cell environment. Further, lack of dynamic control over local stiffness anisotropies and fiber alignment hinders progress in studies in naturally derived fibrous 3D cultures. Here, we present a cell-safe method of patterned photocrosslinking, which can aid in studying biological hypotheses related to mechanotransduction in 3D hydrogels. As previously described by our group, ruthenium-catalyzed photocrosslinking (RCP) of selected ECM regions promotes localized increase in stiffness mediated by focused blue laser light in a confocal microscope. In this study, we further demonstrate that RCP can induce localized strain stiffening and fiber alignment outside of the selected crosslinked region and induce stiffness anisotropy biased towards the direction of fiber alignment. MDA-MB-231 cells are shown to respond to RCP-induced changes in local ECM architecture and display directional bias towards the direction of fiber alignment, as compared to control cells. Further, the effect of patterned crosslinking on a stiffness landscape is measured using multi-axes optical tweezers active microrheology (AMR) with backscattered laser beam illumination. AMR validates RCP as a suitable tool for creating distinct stiffness anisotropies which promote directed migration of cells, further underscoring the usefulness of RCP in cell-ECM studies.

1. Introduction

Cells in the human body reciprocally interact with their local extracellular matrix (ECM). Cells constantly remodel their ECM through synthesis, breakdown, organization, and

crosslinking of ECM proteins and dynamic changes in tension of local ECM fibers [1–3]. Reciprocally, cells also respond to a variety of biochemical and mechanical cues from their ECM. For instance, cells can exhibit contact guidance and migrate along the direction of topographical features on 2D substrates or along the fiber orientation in 3D cultures [4–6]. Contact guidance has been reported to play an important role in numerous physiological processes, including morphogenesis, wound healing and cancer metastasis [5,7–9]. Past research indicates that cells display contact guidance by sensing anisotropy in the organization of local ECM fibers [10]. However, cells also respond to stiffness gradients of their local ECM and migrate towards regions of higher stiffness in a phenomenon known as durotaxis. Durotaxis was shown to be exhibited by different cancer cell lines [11] and it has been previously described to affect cell phenotype and promote fibrosis [12,13].

Despite the importance of cell contact guidance and durotaxis in natural cell behavior, a comprehensive understanding of mechanotransduction and cell-ECM interactions during these biological processes has been elusive. Many studies rely on analysis of cell behavior on 2D substrates [8], which do not reflect a natural cell environment and may provide misleading results as compared those observed in 3D with respect to cell-ECM interactions [2,14]. While micropatterning strategies readily used to generate stiffness gradients in 2D systems have been adapted for synthetic hydrogels [15], they are still emerging for naturally-derived fibrous 3D systems [16]. Approaches developed for 3D cultures include cell-induced hydrogel contraction and fiber alignment [17,18], use of polymers with temperature controlled mechanical properties [19], magnetic alignment of fibrin and collagen fibers [9,10,20,21] or mechanical stretching of hydrogels [22]. All these methods alter fiber alignment and stiffness inside the whole hydrogel, and don't allow the study of individual cell responses to complex changes to their stiffness landscape.

Here, we evaluate a method of patterned photocrosslinking to alter stiffness and fiber alignment and induce directed cell migration at a single cell level. As previously described by our group and others [23–25], the addition of a solution of a ruthenium compound and sodium persulfate promotes fibrin crosslinking in the presence of focused blue laser light in a confocal microscope. Crosslinking of peri-cellular fibrin via ruthenium-catalyzed photocrosslinking (RCP) does not affect cell viability and can precisely be applied to a specified ECM region around an individual cell [23]. Multi-axes optical tweezers active microrheology (AMR) verifies the RCP-induced change in local fiber network stiffness anisotropy. AMR is a non-invasive method of assessing local mechanical properties of a hydrogel. AMR operates by applying optical forces to individual embedded microbeads, and then extracting mechanical properties of the surrounding ECM from the resulting microbead displacements [26]. Past research by our group has shown AMR can be used to measure temporal and spatial changes in ECM-stiffness landscapes around individual cells [27,28] and cell colonies [29]. The optical tweezers are programmed to serially oscillate along six distinct axes passing through the microbead centroid. Bead position is monitored by a detection beam and quadrant photodiode as previously described, and stiffness along each axis is computed from bead displacement and optical force waveforms [27]. Accurate measurements of local stiffness anisotropy with multi-axes AMR aid in describing properties of ECM networks, which were previously shown to be obscured by bulk measurements [27,30].

Past findings reported by our group showed that RCP can promote up to a 25-fold increase in localized ECM stiffness of the crosslinked region as compared to control, with a range of stiffness values corresponding to those naturally established by the cells [23]. Patterned crosslinking was also shown to induce stiffening outside of the crosslinked region, potentially due to strain hardening of the fibers. We postulated that the increase in stiffness outside of the crosslinked region was highly directional and anisotropic. Here, we verify that hypothesis and demonstrate that RCP can be used to create distinct stiffness anisotropies and fiber alignments both inside and outside of the crosslinked region. Furthermore, RCP can induce change in the direction of migration of cells exhibiting contact guidance and durotaxis. Exclusive of the microrheology application presented, this method can be implemented by any investigator with access to a laser scanning confocal microscope.

2.   Materials and Methods

2.1.   Cell culture

Highly invasive and triple-negative human breast cancer cells, MDA-MB-231 (ATCC), were cultured in Dulbecco's Modified Eagle's Medium (DMEM) with low glucose, L-glutamate, and sodium pyruvate (Gibco) supplemented with 10% Fetal Bovine Serum (FBS, Gibco) and 1% penicillin streptomycin (Gibco).

2.2.   Hydrogel preparation

Fibrin hydrogels were prepared at 2.3 mg/ml concentration and incubated at 37 °C and 5% CO_2 for 24 h prior to stiffness measurements and imaging. Bovine stock fibrinogen (Sigma, SLBZ1967) was dissolved in phosphate buffered saline (PBS, Gibco), filtered and mixed with 2 μm carboxylated silica microbeads (0.8 mg/ml, Bangs Laboratories). For hydrogels with cells, 15 k/ml of MDA-MB-231 cells was also added to the solution. Following the addition of bovine thrombin (4 U/ml, Sigma), each solution was polymerized into a 1 ml hydrogel inside of a 35 mm glass bottom dish (MatTek). Hydrogels were incubated for 30 min, and then supplemented with 2 ml of either PBS (cell-free hydrogels) or culture media (hydrogels with cells). On the day of experiments, PBS or culture media was replaced by 2 ml of DMEM with 25 mM HEPES (Gibco), 10% of FBS and 1% penicillin streptomycin.

2.3.   Selective photocrosslinking

Selective photocrosslinking was conducted as previously described [23]. Briefly, 200 μl of culture media with HEPES was substituted with 200 μl of crosslinker solution prepared by mixing 1.5 mg/mL tris(2,20-bipyridyl) dichlororuthenium (II) hexahydrate (Sigma) and 2.4 mg/mL sodium persulfate (Sigma). Photocrosslinking was conducted at least 30 min after the addition of the crosslinker solution, but no later than 6 h. The region of interest (ROI) chosen for crosslinking was selected using built-in functionality of our Fluoview1200 inverted laser scanning confocal microscope (Olympus) into which the optical tweezers active microrheology optics are integrated. The photocrosslinking was induced by illumination of the selected ROI with the 488 nm laser line (0.1 mW) focused by a high numerical aperture microscope objective lens (60x-oil PlanApo TIRFM 1.45NA, Olympus). A selected ROI was crosslinked at a height of 35 μm from the cover glass at a scanning speed of 2 μs/pixel and a total scan resolution of 1600 pixels × 1600 pixels

across the 211.2 μm by 211.2 μm field-of-view (FOV). Circular and rectangular ROIs were crosslinked for 2000 and 500 scans, respectively.

2.4. Microstructural assessment of fibrin hydrogels

Reflection confocal images obtained with the 559 nm laser line were used to quantify the effect of selective photocrosslinking on fiber alignment and pixel brightness. Image contrast was normalized before fiber alignment was measured using the GTFiber software [31]. Pixel brightness of fibers identified by GTFiber software was extracted in MATLAB (The MathWorks Inc.) using custom code. Change in fiber pixel brightness and fiber alignment were calculated in MATLAB by comparing results from images of the same field of view before and after crosslinking. Displacement of fibrin fibers during crosslinking was accessed as previously described [23]. Briefly, optical flow estimation using the Farneback method was performed using the Computer Vision Toolbox™ in MATLAB with the default recommended settings. Optical flow operated on a time series of reflection confocal images. These images were acquired once for every 25 crosslinking scans.

2.5. Active microrheology

Stiffness was measured using our optical tweezers active microrheology system previously described in Jagiełło et al. [27], but optimized to measure material properties in an arbitrary number of directions. Briefly, stiffness of the ECM is probed by oscillating individual microbeads using optical forces applied by a continuous-wave fiber laser with an emission at 1064 nm (YLR-5–1064-LP, IPG Photonics). Trapping beam oscillations are caused by the movement of a pair of galvanometer mirrors (GVS012, ThorLabs), located conjugate to the back focal plane of the microscope objective lens (60x-oil PlanApo TIRFM 1.45NA, Olympus). A detection laser beam of wavelength 785 nm is generated by a single mode fiber-pigtailed laser diode (LP785-SF100, ThorLabs) and co-aligned with the trapping beam at the center of the bead. Change in bead position and trapping beam position are recorded by two quadrant photodiodes (detQPD and trapQPD, 2901 and 2903, respectively, Newport) and used to calculate a complex material response ($a*$) by the relationship X= $a*F$, where X and F are the Fourier components of bead displacement and optical force, respectively. $a*$ is computed once for each oscillation direction under the assumption that $a*$ oscillates purely along that axis. Reported stiffness κ represents the real component of inverse $a*$. Each probed bead was located approximately 35 μm from the cover glass and oscillated along 6 different directions (0, 30, 60, 90, 120 and 150° with respect to the horizontal axis of the camera image FOV). The trapping beam was oscillated with an amplitude of 60 nm and frequency of 50 Hz, unless specified otherwise. The proportionality parameter relating detQPD signals to bead displacements was measured *in situ* per bead and per angle of oscillation. Specifically, the sample is mounted in a stage-top nanopositioning piezoelectric stage (P-545.xR8S PInano® XYPiezoSystem,PI). After centering the stage on each bead, the stage is moved 200 nm across the bead with a constant velocity of 100 nm/s. Recorded detQPD voltages are used to quantify the voltage-to-μm conversion factor [32–34], which is later used to calculate bead displacement during AMR measurements. Prior to AMR measurements in fibrin hydrogels, the AMR system is calibrated in water, as previously described [27,28].

2.6.   Cell tracking experiment

The effect of micropatterned photocrosslinking on migration and orientation of MDA-MB-231 cells was assessed using a Fluoview3000 laser scanning microscope equipped with a 10x-air 0.3 NA microscope objective lens (Olympus). Hydrogels were incubated in a ThermoBox environmental chamber (Tokai Hit) and a stage top incubator (Tokai Hit) with 15% oxygen and 5% CO_2. Photocrosslinking was initiated at least 30 min after the addition of the crosslinking solution to allow for diffusion of the crosslinker solution evenly throughout the hydrogel. Two 1000 μm by 50 μm rectangles separated by 100 μm were selected using built-in functionality of the Fluoview3000 system and crosslinked for 2000 scans using the 488 nm laser line (0.1mW). A selected ROI was crosslinked 100 μm from the cover glass at a scanning speed of 2 μs/pixel and a total scan resolution of 4096 pixels × 4096 pixels across a 1088 μm × 1088 μm FOV. Crosslinking settings were chosen to match the total light energy used in cell-free studies and the Fluoview1200 microscope. Importantly, net fiber displacement as measured by optical flow was shown to be similar in cell and cell-free studies.

Afterwards, the crosslinking solution was washed out three times with fresh media. The fibrin hydrogels were incubated at 37 °C and 5% CO_2 for at least 15 min between the washes to allow for crosslinker diffusion. Next, hydrogels were hydrated with fresh media and returned to the stage top incubator for imaging. Cells between the crosslinked rectangles, and control cells at least 2 mm away from any crosslinked region were then imaged every hour for up to 100 h using the Fluoview3000 with a 4x-air 0.16NA objective lens (Olympus). Cell viability after crosslinking a single 1000 μm by 50 μm rectangle was confirmed with live-dead staining, as described previously [23]. Briefly, 2μM calcein AM (Invitrogen) excited with the 488 nm laser line was used to identify live cells and 4 μM ethidium homodimer (Invitrogen) excited with the 561 nm laser line was used to identify dead cells.

Analysis of cell migration was conducted by first hand-tracing cells in each FOV using Fiji [35]. Afterwards, cell directional bias, cell speed, orientation and direction of cell migration were quantified using a custom MATLAB script. Forward migration index (FMI) was calculated in MATLAB as the average of the ratio of cell displacement in either horizontal (FMI_X) or vertical (FMI_Y) direction to total distance traveled by each cell [11].

2.7.   Principal orientation direction and orientational order parameter

To describe the average orientation of cell migration and alignment, the nematic order parameter and principle orientation were calculated for these vectors [36,37]. The principal orientation direction (director) is calculated as the direction of the principal eigenvector of the mean of the orientation tensors, where the orientation tensor is calculated as the tensor product of a vector with itself. The maximum eigenvalue is rescaled between 0 and 1 and reported as the orientation order parameter (OOP) [38,39]. The director is a measure of the average orientation while OOP describes how well the set of orientations aligns to the director, with 1 meaning a perfect alignment and 0 meaning random orientation.

2.8.   Statistical analysis

Non-parametric statistical analyses at a significance level of 0.05 were conducted to compare non-normally distributed stiffness values ($p < 0.01$, Kolmogorov-Smirnov test). The Friedman test was used to compare stiffness measurements between each oscillation axes. The Kruskal–Wallis test was performed for comparison of multiple groups. The post-hoc Tukey–Kramer test was used to compare specific groups. Distance-dependance of stiffness was described using Spearman's rank correlation coefficient, while change in fiber alignment with distance was compared using ANOVA. The Pearson correlation coefficient was used to quantify the correlation between stiffness and frequency or amplitude of bead oscillation and to assess the time-dependency of cell migration speed. FMI values were compared using Student's t test. All statistical tests were performed in MATLAB.

3.   Results

3.1.   Circular RCP causes radial stiffening

The effect of RCP on stiffening local fibrin networks has been previously described by our group and it was proposed that RCP promotes radial stiffening outside of the crosslinked region [23]. Following enhanced capabilities of our AMR system, we can now test this hypothesis and measure stiffness in an arbitrary number of directions. Here, stiffness (κ) of the fibrin network was measured 24 h after sample preparation by oscillating embedded microbeads at 0°, 30°, 60°, 90°, 120° and 150° with respect to the horizontal axis of the camera (FOV).

In the first set of experiments, a crosslinking solution of ruthenium compound and sodium persulfate was added to 2.3 mg/ml fibrin hydrogels (Fig. 1A) and allowed to diffuse for 30 min. κ within a single FOV was measured along each oscillation axes. These measurements verified that κ of the local fibrin network was isotropic (Friedman test, $p = 0.22$, Fig. 1B–C). Afterwards, a crosslinking reaction was initiated by exposing a 50 μm diameter circular region to the 488 nm laser light for the duration of 500 scans (Fig. 1D, Video S1). As described previously [23–25], 488 nm light is absorbed by the ruthenium compound and initiates the crosslinking reaction by oxidizing tyrosine residues to form a dityrosine crosslink in the presence of sodium persulfate. The effect of crosslinking on stiffness gradients is represented by Figures 1E–F ($n_{beads} = 163$, $n_{sample} = 4$). In Figure 1E, κ at each bead is measured in all 6 directions and represented by a segmented circle with segments that align with the axes of oscillation, and are color-coded for stiffness. For each bead, the axis of largest stiffness is plotted in Figure 1F. Results indicate that after crosslinking, κ within the circular region increased by a factor of 2.11, when comparing median values across all 6 directions. Stiffness within the circular crosslinked region was also found to be isotropic, based on probing 15 beads ($p = 0.15$). Outside of the crosslinked region, κ also increased, although predominantly in the radial direction. Figures 1G–H represent measured κ as a function of distance away from the center of the crosslinked region and the angle by which the axis of AMR oscillation deviates from the radial direction. Stiffness measured along the radial direction is plotted at 0°, while stiffness measured along the tangential direction is plotted at 90°. Before crosslinking, κ was found to be independent of distance from the circle center or deviation angle ($p = 0.52$, Fig. 1G, Table S1). After crosslinking,

stiffness probed up to 30° from the radial direction and as far as 75 μm from the crosslinked region was found to be significantly higher than control stiffness (Fig. 1H). In fact, within this ±30° bin, stiffness of the crosslinked region did not differ significantly from that of regions located up to 25 μm ($p = 0.55$), 25–50 μm ($p = 0.33$) or even 50–75 μm ($p = 0.22$) away from the crosslinked region. In contrast, stiffness probed 60–90° away from the radial direction did not differ from control stiffness (Table S1), regardless of distance away from the crosslinked region center. While radial stiffening did depend to some extent on the duration of crosslinking, a maximum radial stiffening effect was observed with 500 scans, and even after 2000 scans stiffness probed 60–90° away from the radial direction did not differ from the control stiffness (Fig. S1B–C).

During crosslinking, pixel brightness increased for up to 2000 scans (Fig. S1D), predominantly inside the crosslinked region (Fig. 1I). The displacement of fibers during crosslinking was tracked from reflection confocal images (acquired once per 25 crosslinking scans) using optical flow analysis as previously described [23]. During crosslinking, fibers moved radially towards the center of the crosslinked region. The displacement of the fibers was most prominent just outside of the crosslinked region and diminished with distance away from the boundary of the crosslinked region (Fig. 1J,K). Crosslinking with more than 500 scans did not lead to further detectable contraction of the crosslinked region, but the regions outside of the crosslinked region continued to contract (Fig. S2, Video S2).

3.2. Rectangular RCP creates distinct stiffness anisotropies inside and outside of the crosslinked region

Thin rectangular crosslinked regions were also studied due to their intuitive one-dimensional Cartesian symmetry, which was particularly useful when examining the volume between two neighboring crosslinked regions. At first, a single 50 μm by 200 μm rectangular region was crosslinked using the same scanning duration and laser power settings as used for circular regions (Fig. 2A, Video S3). After crosslinking, κ was probed inside and outside of the crosslinked region (Fig. 2B, $n_{beads} = 165$, $n_{sample} = 4$). Control stiffness measurements were conducted before crosslinking, but not necessarily in the same FOV. Figure 1A and first frame of Video S3 are representative of all control conditions before crosslinking. Inside the crosslinked region, κ was found to be higher than control stiffness in all directions, except along the short axis of the rectangle (0°, $p = 0.71$). Stiffness anisotropy in the crosslinked region was observed and κ probed along the long axis of the rectangle (90°) was significantly higher than κ probed along 0° ($p < 0.01$, $n_{beads} = 52$, Table S2). Outside of the crosslinked region, κ measured at 0° was significantly higher than both control stiffness ($p = 0.02$) and stiffness probed at 90° ($p < 0.01$), but not different from κ probed at 0° inside the crosslinked region ($p \gg 0.99$). Direction of the highest stiffness is visualized by arrows in Fig. 2C, indicating diverse anisotropies both inside and outside of the crosslinked region. While stiffness probed at 0° did not show distance-dependency, stiffness probed at 90° decreased with the distance away from the crosslinked region (Fig. S3A; $p < 0.05$). These findings are corroborated by image analysis of fiber architecture before and after crosslinking. Orientation distribution of fibers was measured by processing reflection confocal images in GTFiber software for automated analysis of fibrillar morphologies [31]. After crosslinking, the crosslinked region showed a bias towards 90° fiber orientation (Fig.

2D). Change in fiber alignment was not detected outside of the crosslinked region when considering that region as a whole, or binning it into regions located 0–50, 50–100, and 100–150 μm away from the crosslinked region (repeated measures ANOVA; $p = 0.70$, Fig. S3B). Pixel brightness increased notably inside the crosslinked region, a finding consistent with our previous work [23] (Fig. 2E). An increase in pixel brightness was also observed outside of the crosslinked region, although to a lesser extent. Pixel brightness decreased significantly with distance away from the crosslinked region (Spearman's rank correlation coefficient, $r_s = -0.62$, $p <0.01$). Fiber displacements outside of the crosslinked region were primarily towards the crosslinked region (Fig. 2F, Video S4) and predominantly in the horizontal direction. Similar to trends observed after crosslinking the circular region, maximum displacement of fibers was detected at the edge of the crosslinked rectangular region.

3.3. Pairs of rectangular crosslinked regions

In order to establish more pronounced stiffness anisotropies, two 50 μm by 200 μm rectangles were crosslinked parallel to one another (Fig 3A, Video S3). Rectangles were separated by either 50 μm (defined as R50) or 100 μm (defined as R100). After each treatment, κ was significantly higher than control stiffness in all directions, both inside and outside of the crosslinked regions ($p <0.01$, Table S2). Stiffness in crosslinked regions was comparable between R50 and R100 treatments (Fig. 3B–C), as is also true for the non-crosslinked regions. For both R50 and R100, stiffness anisotropy was biased towards 90° inside the crosslinked regions, but towards 0° between the crosslinked regions. Interestingly, stiffness measured along the 0° direction did not change with the horizontal coordinate of probed beads. This holds true within and between the crosslinked regions. This result is in agreement with that observed up to 110 μm away from a single crosslinked rectangle (Fig. 2B). However, κ within each crosslinked region was higher in the case of two crosslinked rectangles as compared to a single rectangle (with the exception of κ probed at 90°; Table S2). Similarly, when comparing regions equidistant from a crosslinked rectangle and probed at 0°, R50 and R100 treatments resulted in higher stiffness between the crosslinked rectangles than stiffness measured in regions adjacent to a single crosslinked rectangle (Table S3).

An additional experiment was conducted to assess the extent by which AMR measurements of κ were frequency or bead-displacement amplitude dependent. AMR was conducted at different frequencies and amplitudes of bead oscillations following single rectangle, R50, or R100 crosslinking treatment. Stiffness was not significantly correlated with oscillation amplitudes ranging between 40 and 80 nm (Fig. S4), and was mostly independent of oscillation frequencies between 20 and 200 Hz (Fig. S5). The Pearson correlation coefficient r did not exceed $r = -0.19$ and $r = 0.15$ for amplitude and frequency testing, respectively.

Fiber alignment after crosslinking either one or two rectangles was subtle and not evident without computational image analysis. Analysis in GTFiber software indicated that crosslinking two rectangles instead of one resulted in similar alignment inside the crosslinked region, but more prominent horizontal alignment outside of crosslinked regions (Fig. 3D). In all cases fiber alignment was biased towards the 90° orientation inside the

crosslinked region and towards the 0° orientation outside of the crosslinked region. After both R50 and R100 treatments, pixel brightness was higher inside the crosslinked regions, than between them (Fig. 3E). Fiber displacement during crosslinking varied in time. During the first 50 crosslinking scans fibers moved towards the center of the crosslinked region. With further crosslinking, fiber displacement was observed towards the center of the region between the crosslinked rectangles (Fig. 3F–G, Video S4).

3.4.   RCP induces changes in cell migration

Next, the effect of patterned photocrosslinking on direction of cell migration was evaluated in fibrin hydrogels containing MDA-MB-231 cells. MDA-MB-231 human breast cancer cells are known to respond to stiffness gradients in 2D and 3D cultures and were previously shown to display positive durotaxis [11,40,41]. Here, two 1000 μm × 50 μm rectangles spaced by 100μm were crosslinked for 2000 scans using the 488 nm laser line of a Fluoview3000 microscope. Rectangles were oriented vertically with respect to the field of view (Fig. 4A). Unlike the Fluoview1200 system used for AMR measurements, the Fluoview3000 is equipped with a stage top incubator for multi-day studies. Cells were observed every hour for up to 100 h following crosslinking (n_{cells} = 15, Fig. 4A; e.g. Video S5). Control cells were imaged similarly (n_{cells} = 25, Fig. 4A; e.g. Video S6).

Cells between the crosslinked regions were found to migrate at lower speeds than control cells ($p < 0.01$, Fig. 4B). Cells located centrally between the crosslinked regions were more likely to move in the horizontal direction (directional bias < 0, Fig. 4C) than in the vertical direction. However, as cells moved closer to the crosslinked region, they exhibited a vertical directional bias (directional bias > 0). Similarly, cells located in the central region exhibit horizontal-dominant direction of cell orientation (Fig. 4D) and cell migration (Fig. 4E). These trends transition to vertical near to the crosslinked rectangles. Forward migration indices (FMI) did not differ from 0 for control cells in either horizontal (FMI_X; $p = 0.72$, Fig. 4G) or vertical (FMI_Y; $p = 0.26$) direction. In contrast, cells between the crosslinked regions had higher FMI_X than control cells ($FMI_X = 0.23$, $p < 0.01$), while FMI_Y in the vertical direction ($FMI_Y = 0.12$) did not differ from control FMI_Y ($p = 0.29$).

4.   Discussion

In this study we verified ruthenium-catalyzed photocrosslinking (RCP) as a suitable tool for creating distinct stiffness landscapes and anisotropies, both inside and outside of crosslinked regions. The use of multi-axes AMR allowed us to assess relationships between fiber alignment and stiffness anisotropy, where such properties are not accessible using surface probe technologies, single axis AMR, or bulk measurements. Crosslinking a circular region resulted in radial stiffening towards the center of the crosslinked region. Stiffness inside the crosslinked region was found to be isotropic and 2.1-fold higher than before crosslinking. Fold-increase in stiffness after RCP was comparable with the effect of magnetic alignment of fibers [10] and with other methods of creating stiffness gradients in natural hydrogels [42]. A more in-depth analysis of the RCP effect on fiber displacement was done in this study as compared to our previous study [22]. The method of optical flow analysis was used to calculate the displacement field within and surrounding crosslinked regions.

The direction of greatest displacement corresponded to the axis of highest stiffness. Optical flow analysis of fiber displacement indicates that the circular crosslinked region approached maximal contraction by 500 scans. While additional fiber displacement within the crosslinked region was not detected beyond 500 crosslinking scans, displacement outside of the crosslinked region was still changing after 2000 scans. This trend is in contrast with stiffness measurements by AMR, which found no significant difference in stiffness after 500, 1000 and 2000 crosslinking scans. Given that the stiffness values are well within the limit of AMR measurement, we are likely observing a low-strain effect that does not significantly contribute to further strain hardening.

In order to further investigate RCP effect on local ECM changes, different crosslinked geometries were explored. Rectangular crosslinking promoted stiffening and fiber alignment inside the crosslinked region biased along the long axis of the rectangle. Outside of the crosslinked region, the reverse bias was observed up to 110 μm away from the crosslinked rectangle, suggesting that the region is under tension and RCP may induce strain hardening. Interestingly, stiffness measured in the horizontal direction (0°) did not change with probed bead location indicating lack of measurable spatial gradients (Fig. S3A, S6). The lack of distance-dependent stiffness gradients probed at 0° is consistent with strain hardening where as seen in Figure 3G, the fiber displacement gradient along the horizontal axis is fairly constant throughout the region, indicating constant strain level. In contrast, stiffness gradients with respect to the horizontal axis of the image were detected when stiffness was measured along 60°, 90° and 120° direction (Fig. S3A, S6). Optical flow analysis during crosslinking rectangles found that the derivative of horizontal displacement with horizontal position is positive in the non-crosslinked regions (Figs. 2G, 3G), indicating that the material is being stretched, which is consistent with the observed increase in stiffness following crosslinking, and suggestive of strain hardening in that region. A more comprehensive analysis relating displacements to strain hardening requires a 3D consideration of fiber displacements and dynamic axial focusing of the optical tweezers, which are currently being developed by our group.

Crosslinking two rectangles instead of one resulted in higher stiffness and a greater change in fiber alignment. Surprisingly, we found pixels in between the crosslinked regions to be brighter for R50 as compared to R100. Such differences in pixel brightness could be indicative of diffusion of the crosslinking radicals from the laser-scanned region. However, crosslinking results in a detectable autofluorescence (Ex: 561 nm, Em: 570–670 nm) and only fibers in the selected laser-scanned region had detectable signal, suggesting that chemical alterations were highly localized (Fig. S7E).

MDA-MB-231 cells exhibited behavior consistent with contact guidance along a network of fibers aligned by micropatterned RCP. The cells favored horizontal migration between the crosslinked rectangles where fibers were biased towards the horizontal direction (Fig. 4C). As cells approached the crosslinked regions with fibers exhibiting more vertical orientation, they orientated themselves accordingly. Similarly, cell orientation was shown to correspond with the axis of the highest stiffness. Our experiments show that not only were fibers aligned, but stiffness was anisotropic, and these 'off-axis' stiffness values did exhibit gradients in the horizontal direction (Fig. S6). In consideration of biophysical cues,

it is possible that effects of contact guidance were supplemented by these gradients, a phenomena currently being investigated by our group.

Changes in fiber alignments introduced by RCP are quite subtle, and significantly less prominent than changes caused by magnetic alignment of fibers [9,20,21] or mechanical stretching of hydrogels [22]. Nonetheless, observed changes in migratory behaviour and alignment of MDA-MB-231 cells indicate that the effect of RCP on fiber alignment and stiffness landscape is strong enough to promote directed cell migration. Moreover, unlike other existing methods, RCP can alter stiffness landscape and anisotropy around individual cells embedded inside 3D fibrous hydrogels and allows for observation of a single cell's response to changes in local ECM physical properties. Relevant to such studies, the extent of stiffness anisotropy and fiber alignment can be readily controlled by crosslinking duration, delivered light dose, photoinitiator concentration or by modifying the geometry of the crosslinked region. Further, compared to commonly used crosslinking techniques developed for synthetic hydrogels [43,44] or riboflavin-based crosslinking of naturally-derived fibrous hydrogels [45], RCP does not require the use of ultraviolet (UV) light. RCP can be induced using a 488 nm laser line, which is safer for cells and readily available in most confocal laser scanning microscopes.

5. Conclusion

In this study, multi-axes AMR and analysis of reflection confocal microscopy images were used to assess the effect of micropatterned ruthenium-catalyzed photocrosslinking on local ECM stiffness anisotropy, fiber alignment and displacement. We verified that RCP can be applied to establish distinct local stiffness anisotropies in adjacent regions. Cells were shown to respond to RCP-mediated changes and exhibited directed cell migration congruent with fiber alignment direction, axis of greatest stiffness, and in a direction for which off-axis stiffness values do exhibit spatial gradients. The usefulness of RCP in cell-ECM studies is further underscored by its wide availability to most investigators and applicability to fibrous 3D hydrogels and other strain-hardening materials.

Supplementary Material

Refer to Web version on PubMed Central for supplementary material.

Acknowledgements

References

[1]. Malandrino A, Trepat X, Kamm RD, Mak M, Dynamic filopodial forces induce accumulation, damage, and plastic remodeling of 3D extracellular matrices, PLoS Comput. Biol. 15 (2019) 1–26. 10.1371/journal.pcbi.1006684.

[2]. Doyle AD, Yamada KM, Mechanosensing via cell-matrix adhesions in 3D microenvironments., Exp. Cell Res. 343 (2015) 1–7. 10.1016/j.yexcr.2015.10.033.

[3]. Kular JK, Basu S, Sharma RI, The extracellular matrix : Structure, composition, age-related differences, tools for analysis and applications for tissue engineering, (2014). 10.1177/2041731414557112.

[4]. Linke P, Suzuki R, Yamamoto A, Nakahata M, Kengaku M, Fujiwara T, Ohzono T, Tanaka M, Dynamic Contact Guidance of Myoblasts by Feature Size and Reversible Switching of Substrate Topography: Orchestration of Cell Shape, Orientation, and Nematic Ordering of Actin Cytoskeletons, Langmuir. 35 (2019) 7538–7551. 10.1021/acs.langmuir.8b02972. [PubMed: 30376342]

[5]. Ramirez-San Juan GR, Oakes PW, Gardel ML, Contact guidance requires spatial control of leading-edge protrusion, Mol. Biol. Cell. 28 (2017) 1043–1053. 10.1091/mbc.E16-11-0769. [PubMed: 28228548]

[6]. Ray A, Lee O, Win Z, Edwards RM, Alford PW, Kim DH, Provenzano PP, Anisotropic forces from spatially constrained focal adhesions mediate contact guidance directed cell migration, Nat. Commun. 8 (2017). 10.1038/ncomms14923.

[7]. Nuhn JAM, Perez AM, Schneider IC, Contact guidance diversity in rotationally aligned collagen matrices, Acta Biomater. 66 (2018) 248–257. 10.1016/j.actbio.2017.11.039. [PubMed: 29196116]

[8]. Leclech C, Villard C, Cellular and Subcellular Contact Guidance on Microfabricated Substrates, Front. Bioeng. Biotechnol 8 (2020) 1–30. 10.3389/fbioe.2020.551505. [PubMed: 32039188]

[9]. Kim J, Cao Y, Eddy C, Deng Y, Levine H, Rappel WJ, Sun B, The mechanics and dynamics of cancer cells sensing noisy 3D contact guidance, Proc. Natl. Acad. Sci. U. S. A. 118 (2021) 1–8. 10.1073/pnas.2024780118.

[10]. Thrivikraman G, Jagiełło A, Lai VK, Johnson SL, Keating M, Nelson A, Schultz B, Wang CM, Levine AJ, Botvinick EL, Tranquillo RT, Cell contact guidance via sensing anisotropy of network mechanical resistance, Proc. Natl. Acad. Sci. U. S. A. 118 (2021) 1–11. 10.1073/pnas.2024942118.

[11]. DuChez BJ, Doyle AD, Dimitriadis EK, Yamada KM, Durotaxis by Human Cancer Cells, Biophys. J. 116 (2019) 670–683. 10.1016/j.bpj.2019.01.009. [PubMed: 30709621]

[12]. Lo CM, Wang HB, Dembo M, Wang YL, Cell movement is guided by the rigidity of the substrate, Biophys. J. 79 (2000) 144–152. 10.1016/S0006-3495(00)76279-5. [PubMed: 10866943]

[13]. Sunyer R, Conte V, Escribano J, Elosegui-Artola A, Labernadie A, Valon L, Navajas D, García-Aznar JM, Muñoz JJ, Roca-Cusachs P, Trepat X, Collective cell durotaxis emerges from long-range intercellular force transmission, Science (80-.). 353 (2016) 1157–1161. 10.1126/science.aaf7119.

[14]. Jensen C, Teng Y, Is It Time to Start Transitioning From 2D to 3D Cell Culture?, Front. Mol. Biosci 7 (2020) 1–15. 10.3389/fmolb.2020.00033. [PubMed: 32039235]

[15]. Whang M, Kim J, Synthetic hydrogels with stiffness gradients for durotaxis study and tissue engineering scaffolds, Tissue Eng. Regen. Med. 13 (2016) 126–139. 10.1007/s13770-016-0026-x. [PubMed: 30603392]

[16]. D'Arcangelo E, McGuigan AP, Micropatterning strategies to engineer controlled cell and tissue architecture in vitro, Biotechniques. 58 (2015) 13–23. 10.2144/000114245. [PubMed: 25605576]

[17]. Ray A, Slama ZM, Morford RK, Madden SA, Provenzano PP, Enhanced Directional Migration of Cancer Stem Cells in 3D Aligned Collagen Matrices, Biophys. J. 112 (2017) 1023–1036. 10.1016/j.bpj.2017.01.007. [PubMed: 28297639]

[18]. Morin KT, Tranquillo RT, Guided sprouting from endothelial spheroids in fibrin gels aligned by magnetic fields and cell-induced gel compaction, Biomaterials. 32 (2011) 6111–6118. 10.1016/j.biomaterials.2011.05.018. [PubMed: 21636127]

[19]. Jin Y, Yang T, Ju S, Zhang H, Choi TY, Neogi A, Thermally tunable dynamic and static elastic properties of hydrogel due to volumetric phase transition, Polymers (Basel). 12 (2020). 10.3390/polym12071462.

[20]. Namani R, Wood MD, Sakiyama-Elbert SE, Bayly PV, Anisotropic mechanical properties of magnetically aligned fibrin gels measured by magnetic resonance elastography, J. Biomech. 42 (2009) 2047–2053. 10.1016/j.jbiomech.2009.06.007. [PubMed: 19656516]

[21]. Taufalele PV, VanderBurgh JA, Muñoz A, Zanotelli MR, Reinhart-King CA, Fiber alignment drives changes in architectural and mechanical features in collagen matrices, PLoS One. 14 (2019) 1–11. 10.1371/journal.pone.0216537.

[22]. Nam E, Lee WC, Takeuchi S, Formation of Highly Aligned Collagen Nanofibers by Continuous Cyclic Stretch of a Collagen Hydrogel Sheet, Macromol. Biosci. (2016) 995–1000. 10.1002/mabi.201600068. [PubMed: 27136124]

[23]. Keating M, Lim M, Hu Q, Botvinick E, Selective stiffening of fibrin hydrogels with micron resolution via photocrosslinking, Acta Biomater. 87 (2019) 88–96. 10.1016/j.actbio.2019.01.034. [PubMed: 30660778]

[24]. Bjork J, Johnson S, Tranquillo R, Ruthenium-catalyzed photo cross-linking of fibrin-based engineered tissue, Biomaterials. 32 (2011) 2479–2488. [PubMed: 21196047]

[25]. Fancy DA, Kodadek T, Chemistry for the analysis of protein-protein interactions: Rapid and efficient cross-linking triggered by long wavelength light, Proc. Natl. Acad. Sci. U. S. A. 96 (1999) 6020–6024. 10.1073/pnas.96.11.6020. [PubMed: 10339534]

[26]. Mizuno D, Head DA, MacKintosh FC, Schmidt CF, Active and passive microrheology in equilibrium and nonequilibrium systems, Macromolecules. 41 (2008) 7194–7202. 10.1021/ma801218z.

[27]. Jagiełło A, Lim M, Botvinick E, Dermal fibroblasts and triple-negative mammary epithelial cancer cells differentially stiffen their local matrix, APL Bioeng 4 (2020). 10.1063/5.0021030.

[28]. Keating M, Kurup A, Alvarez-Elizondo M, Levine AJ, Botvinick E, Spatial distributions of pericellular stiffness in natural extracellular matrices are dependent on cell-mediated proteolysis and contractility, Acta Biomater. 57 (2017) 304–312. 10.1016/j.actbio.2017.05.008. [PubMed: 28483696]

[29]. Juliar BA, Keating MT, Kong YP, Botvinick EL, Putnam AJ, Sprouting angiogenesis induces signi fi cant mechanical heterogeneities and ECM stiffening across length scales in fi brin hydrogels, Biomaterials. 162 (2018) 99–108. 10.1016/j.biomaterials.2018.02.012. [PubMed: 29438884]

[30]. Jones CAR, Cibula M, Feng J, Krnacik EA, McIntyre DH, Levine H, Sun B, Micromechanics of cellularized biopolymer networks, Proc. Natl. Acad. Sci. U. S. A. 112 (2015) E5117–E5122. 10.1073/pnas.1509663112. [PubMed: 26324923]

[31]. Persson NE, McBride MA, Grover MA, Reichmanis E, Automated analysis of orientational order in images of fibrillar materials, Chem. Mater. 29 (2017) 3–14. 10.1021/acs.chemmater.6b01825.

[32]. Allersma MW, Gittes F, DeCastro MJ, Stewart RJ, Schmidt CF, Two-Dimensional Tracking of ncd Motility by Back Focal Plane Interferometry, Biophys. J. 74 (1998) 1074–1085. 10.1016/S0006-3495(98)74031-7. [PubMed: 9533719]

[33]. Staunton JR, Vieira W, Fung KL, Lake R, Devine A, Tanner K, Mechanical Properties of the Tumor Stromal Microenvironment Probed In Vitro and Ex Vivo by In Situ-Calibrated Optical Trap-Based Active Microrheology, Cell. Mol. Bioeng. 9 (2016) 398–417. 10.1007/s12195-016-0460-9. [PubMed: 27752289]

[34]. Blehm BH, Devine A, Staunton JR, Tanner K, In vivo tissue has non-linear rheological behavior distinct from 3D biomimetic hydrogels, as determined by AMOTIV microscopy, Biomaterials. 83 (2016) 66–78. 10.1016/j.biomaterials.2015.12.019. [PubMed: 26773661]

[35]. Schindelin J, Arganda-Carreras I, Frise E, Kaynig V, Longair M, Pietzsch T, Preibisch S, Rueden C, Saalfeld S, Schmid B, Tinevez JY, White DJ, Hartenstein V, Eliceiri K, Tomancak P, Cardona A, Fiji: An open-source platform for biological-image analysis, Nat. Methods 9 (2012) 676–682. 10.1038/nmeth.2019. [PubMed: 22743772]

[36]. Meier G, Saupe A, Dielectric Relaxation in Nematic Liquid Crystals Dielectric Relaxation in Nematic Liquid Crystals, 1152 (2007). 10.1080/15421406608083290.

[37]. Chaikin PM, Lubensky TC, Book Review : Principles of Condensed Matter Physics, (2014). 10.1007/BF02179565.

[38]. Umeno S, A., Kotani H, Iwasaka M, and Ueno, Quantification of adherent cell orientation and morphology under strong magnetic fields, IEEE Trans. Magn. 37 (2001) 2909–2911. 10.1109/20.951344.

[39]. Altair T, Id M, Id JN, Fibben KS, Kong X, Id TK, Yokomori K, Id AG, Striated myocyte structural integrity : Automated analysis of sarcomeric z-discs, (2020) 1–21. 10.1371/journal.pcbi.1007676.

[40]. Ansardamavandi A, Tafazzoli-shadpour M, Ali M, Group F, Behavioral remodeling of normal and cancerous epithelial cell lines with differing invasion potential induced by substrate elastic modulus, Cell Adh. Migr 12 (2018) 472–488. 10.1080/19336918.2018.1475803. [PubMed: 29969940]

[41]. Riching KM, Cox BL, Salick MR, Pehlke C, Riching AS, Ponik SM, Bass BR, Crone WC, Jiang Y, Weaver AM, Eliceiri KW, Keely PJ, 3D collagen alignment limits protrusions to enhance breast cancer cell persistence, Biophysj. 107 (2014) 2546–2558. 10.1016/j.bpj.2014.10.035.

[42]. Chang CY, Lin CC, Hydrogel models with stiffness gradients for interrogating pancreatic cancer cell fate, Bioengineering. 8 (2021) 1–18. 10.3390/bioengineering8030037.

[43]. Djordjevic DM, Cirkovic ST, Mandic DS, Biomedical applications, Magn. Ferroelectr. Multiferroic Met. Oxides. (2018) 411–430. 10.1016/B978-0-12-811180-2.00020-7.

[44]. Eke G, Mangir N, Hasirci N, MacNeil S, Hasirci V, Development of a UV crosslinked biodegradable hydrogel containing adipose derived stem cells to promote vascularization for skin wounds and tissue engineering, Biomaterials. 129 (2017) 188–198. 10.1016/j.biomaterials.2017.03.021. [PubMed: 28343005]

[45]. Tirella A, Liberto T, Ahluwalia A, Riboflavin and collagen: New crosslinking methods to tailor the stiffness of hydrogels, Mater. Lett. 74 (2012) 58–61. 10.1016/j.matlet.2012.01.036.
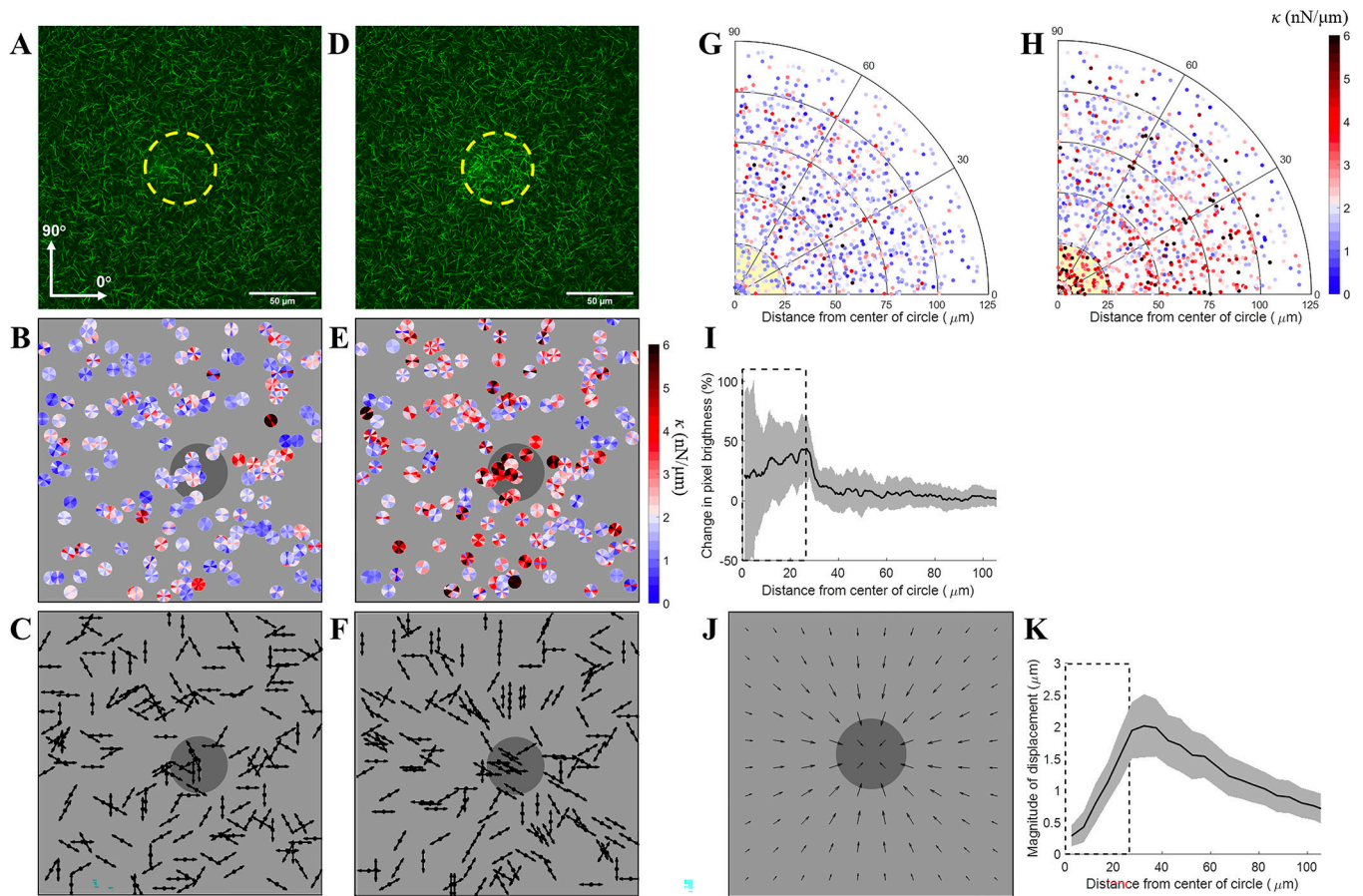
Fig. 1.
The effect of crosslinking a circular region. (A, D) Reflection confocal images before (A) and after (D) crosslinking a circular region marked by the yellow dashed line. Stiffness was probed in 6 directions using multi-axes AMR before (B) and after (E) crosslinking. Stiffness is color-coded separately for each direction of bead oscillation. Crosslinked region is marked by a dark gray background. (C, F) Direction of the highest stiffness is represented by arrows before (C) and after (F) crosslinking. (G, H) Change in stiffness with the distance away from the crosslinked circle center (yellow background) and angle of deviation of probed bead position from the radial direction before (G) and after (H) crosslinking. (I) Change in pixel brightness with distance from the crosslinked circle center. Crosslinked region is denoted by dashed rectangle. Median IQR. (J-K) Optical flow detects matrix deformation during crosslinking.
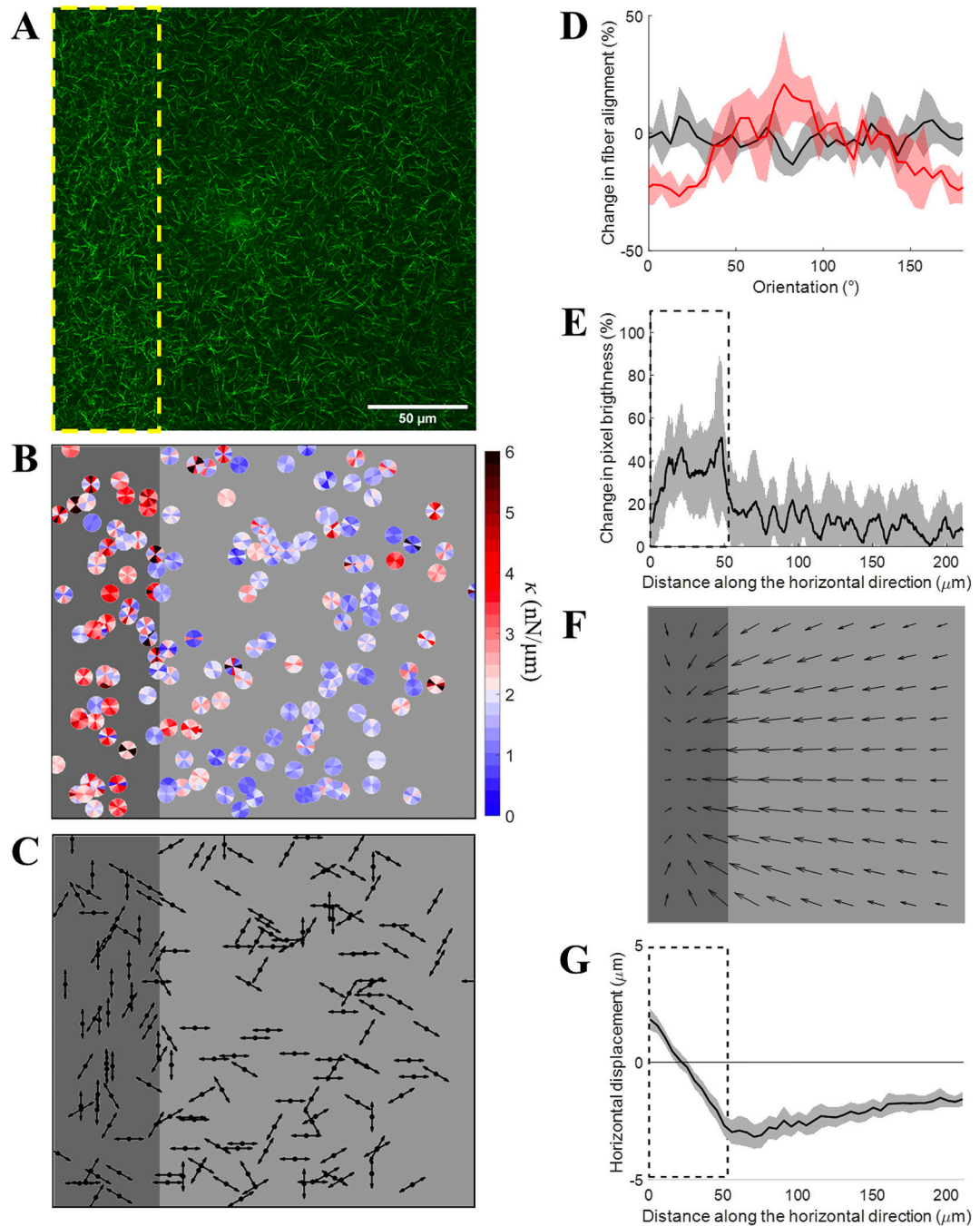
Fig. 2.
The effect of crosslinking a rectangular region. (A) Reflection confocal image after crosslinking a region marked by the yellow dashed line. (B) Stiffness was probed in 6 directions using multi-axes AMR Stiffness is color-coded separately for each direction of bead oscillation. Crosslinked region is marked by a dark gray background. (C) Direction of the highest stiffness is represented by arrows. (D) Fiber alignment within (red) and beyond (black) the crosslinked region. (E) Change in pixel brightness with distance from the

crosslinked region (denoted by dashed rectangle). Median ± IQR. (F-G) Optical flow detects matrix deformation.
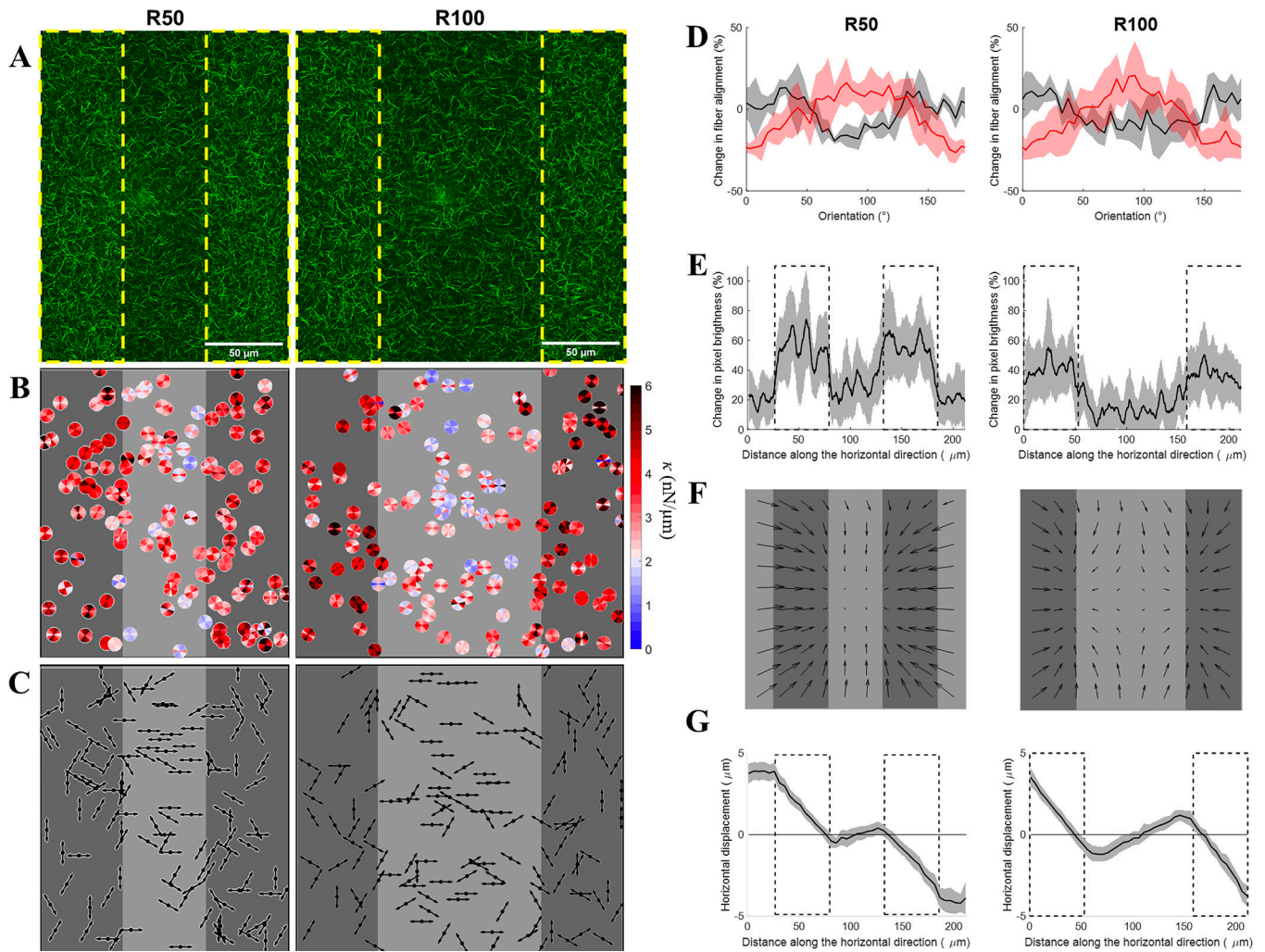
Fig. 3.
The effect of crosslinking two rectangular regions. (A) Reflection confocal images after crosslinking rectangles separated by 50 μm (R50) or 100 μm (R100) - marked by the yellow dashed lines. (B) Stiffness was probed in 6 directions using multi-axes AMR. Stiffness is color-coded separately for each direction of bead oscillation. Crosslinked region is marked by a dark gray background. (C) Direction of the highest stiffness is represented by arrows. (D) Fiber alignment within (red) and beyond (black) the crosslinked region. (E) Change in pixel brightness with distance from the crosslinked region (denoted by dashed rectangle). Median ± IQR. (F-G) Optical flow detects matrix deformation.
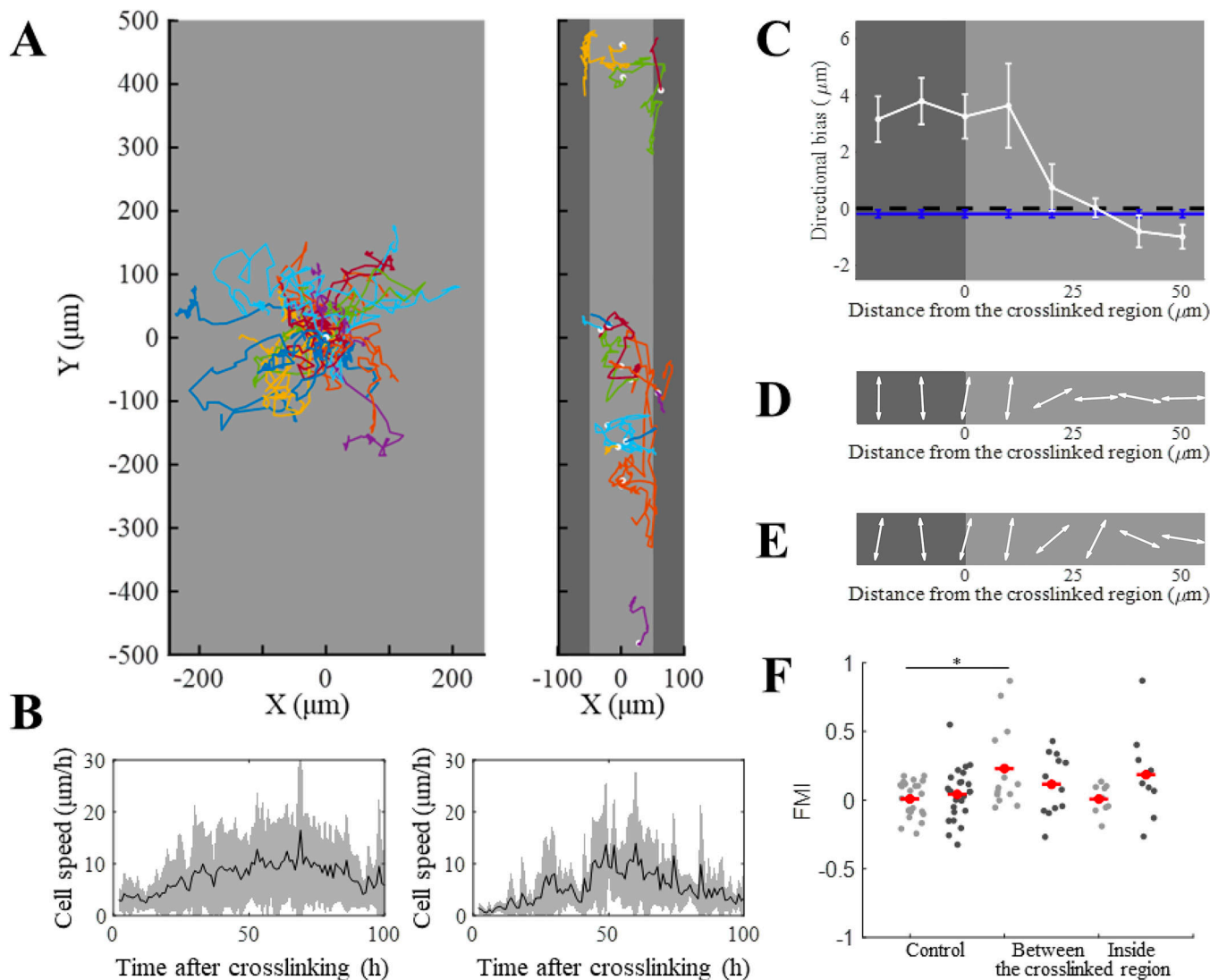
Fig. 4.
RCP induces changes in migratory behavior of MDA-MB-231 cells. (A) Trajectories of
control cells (left) and cells between (right) the crosslinked rectangular regions (dark gray).
(B) Change in average cell speed with time after crosslinking, calculated between every 1 h
for control cells (left) and cells between the crosslinked regions (right). (C) Directional bias
defined as a difference in absolute displacement in the vertical and horizontal direction for
control cells (blue line) and cells between the crosslinked regions (white line). (D) Dominant
cell orientation and (E) dominant direction of cell migration, represented with respect to
the distance away from the crosslinked region and binned for every 10 μm (F) FMI index
values for each cell in the direction perpendicular (light grey background) and parallel (dark
grey background) to the crosslinked region. Mean FMI values are denoted by red markers; *
denotes statistical significance.